ELSEVIER

Contents lists available at ScienceDirect

Materials & Design

journal homepage: www.elsevier.com/locate/matdes



Prediction of tensile performance for 3D printed photopolymer gyroid lattices using structural porosity, base material properties, and machine learning



Jacob Peloquin ^{a,*}, Alina Kirillova ^c, Cynthia Rudin ^b, L.C. Brinson ^a, Ken Gall ^a

- ^a Department of Mechanical Engineering and Materials Science, Duke University, Durham, NC 27708, USA
- ^b Department of Computer Science, Duke University, Durham, NC 27708, USA
- ^c Department of Materials Science and Engineering, Iowa State University, Ames, IA 50011, USA

HIGHLIGHTS

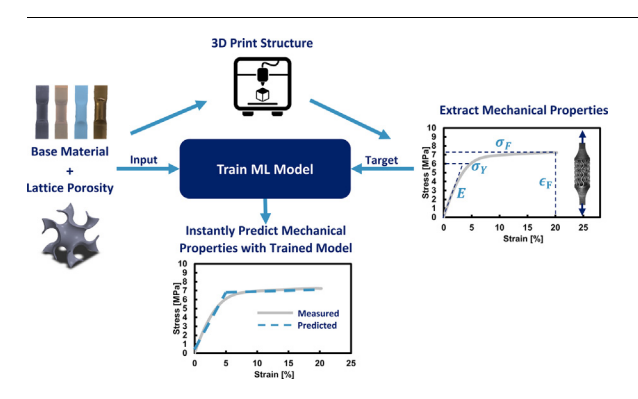
- The ability of a simple machine learning model to predict mechanical properties of 3D printed lattices is demonstrated.
- The effect of printing defects on photopolymer lattice sample mechanical and geometric properties is highlighted.
- A framework is presented for including both structure and material info into property predictions of 3D printed lattices.
- Kernel ridge regression is used to make accurate mechanical property predictions using a small amount of training data.

ARTICLE INFO

Article history: Received 15 April 2023 Revised 14 June 2023 Accepted 26 June 2023 Available online 27 June 2023

Keywords:
Machine learning
Mechanical performance
Lattice structures
Diverse materials
Additive manufacturing

G R A P H I C A L A B S T R A C T



ABSTRACT

Advancements in additive manufacturing (AM) technology and three-dimensional (3D) modeling software have enabled the fabrication of parts with combinations of properties that were impossible to achieve with traditional manufacturing techniques. Porous designs such as truss-based and sheet-based lattices have gained much attention in recent years due to their versatility. The multitude of lattice design possibilities, coupled with a growing list of available 3D printing materials, has provided a vast range of 3D printable structures that can be used to achieve desired performance. However, the process of computationally or experimentally evaluating many combinations of base material and lattice design for a given application is impractical. This research proposes a framework for quickly predicting key mechanical properties of 3D printed gyroid lattices using information about the base material and porosity of the structure. Experimental data was gathered to train a simple, interpretable, and accurate kernel ridge regression machine learning model. The performance of the model was then compared to numerical simulation data and demonstrated similar accuracy at a fraction of the computation time. Ultimately, the model development serves as an advancement in ML-driven mechanical property prediction that can be used to guide extension of current and future models.

© 2023 The Authors. Published by Elsevier Ltd. This is an open access article under the CC BY-NC-ND license (http://creativecommons.org/licenses/by-nc-nd/4.0/).

E-mail address: jake.peloquin@duke.edu (J. Peloquin).

^{*} Corresponding author.

1. Introduction

The bounds of what is possible with additive manufacturing (AM) continue to be pushed by advancements in both threedimensional (3D) printing technology and 3D modeling software. Methods such as designing porous geometries, tuning the composition of heterogeneous mixtures, and doping materials with particulates have been used to achieve 3D printed structures with superior mechanical properties and tailored functionality [1-12]. These structures are used in applications where either a custom fit is necessary or the design is unmanufacturable with traditional methods. For example, 3D printed products can be seen used in hospitals and surgeries as orthopedic implants for promoting bone ingrowth and fitting the patient's specific anatomy [13]. The innumerable possibilities enabled by these advancements motivate the development of faster ways to assess structure performance and determine optimal structure design and material composition for a given requirement.

Cellular lattices have been widely incorporated into products such as orthopedic devices, aerospace components, and heat exchangers due to their high load-bearing strength, lightweight capabilities, osseointegration, and thermal insulation properties [14–18]. These lattices are often identified as having either stochastic or periodic porosity. Porosity will be defined hereafter as the percentage of the volume that is void space within the lattice. Lattices with stochastic porosity contain randomly distributed and sized pores, and those with periodic porosity contain repeated unit cells of uniform pore size and distribution. Periodic lattice designs have been shown to mechanically outperform stochastic lattice designs, and the uniformity of their pore distribution allows for precise tuning of geometric properties by adjusting the cell size, wall thickness, and volume fraction of the lattice [19–25]. Due to the intricate geometry of these lattices, traditional manufacturing techniques such as machining and injection molding are impractical, and AM techniques have been adopted to achieve these desired geometries [26-32]. Researchers have found success 3D printing periodic lattices for varied materials, yet the process of modeling, printing, and testing the wide array of designs is prohibitive when many different variations of the lattice need to be explored [1,3,5,20].

One method to expedite discovery of these structures is direct numerical simulation such as finite element analysis (FEA). Using FEA, a computerized 3D design can be subjected to simulated environmental conditions, and the response of the design to the conditions is then calculated. Calculating the theoretical stress-strain curve of a design is a common objective of using FEA [33–36]. The design is spatially constrained and subjected to an external force, and the deformation and internal stress of the part are calculated. However, FEA is computationally intensive for complex designs [37] and can require a significant amount of time to produce results for each new design of interest. Furthermore, FEA is often unable to account for the impact of imperfections that can occur when 3D printing. These imperfections, such as postprocessing defects or printing defects, can lead to inaccurate sample geometry and expedited or inconsistent part failure, and are crucial to consider with models of 3D printed objects [38–45].

Machine learning (ML) algorithms have become a popular method for creating models to predict the mechanical performance of structures [46–50]. Algorithms have been used to create models that predict mechanical properties and even entire stress–strain curves of periodic lattice structures, 2D composites, and phase-separated structures [21,51–55]. Gu et al. [54] demonstrated the ability to predict 2D composite designs that exhibit optimal strength and toughness using deep learning (DL) and a trained convolutional neural network (CNN). FEA simulation was used to

create a dataset mapping the geometry of the composite structure to its mechanical properties observed during tensile loading. The 2D composite designs used to train the model each consisted of a random grid arrangement of squares representing either high or low relative material stiffness. By learning the relationship between grid arrangement and mechanical properties, the model was able to generate an arrangement of grid components with optimized strength and toughness. Yang et al. [55] built upon this work to develop a model capable of predicting the entire stressstrain behavior of such 2D composites using principal component analysis (PCA) and CNN. The stress-strain data calculated for each composite using FEA is transformed into a reduced order latent space using PCA, and the CNN model then makes predictions in this new space with a high degree of accuracy. Hassanin et al. [21] successfully used DL to predict the stress-strain curve of a 3D printed titanium diamond lattice structure. The structures were printed and physically tested in compression to extract the stress-strain data, and after training, the model was able to predict the stressstrain curve of the structure based on solely the strut length, strut diameter, and strut orientation angle of the diamond lattice. Wang et al. [56] introduced a method for predicting the peak force, displacement at peak force, mean crushing force, and effective compression stroke of braided textile-reinforced tubular structures consisting of carbon fiber bundles and an epoxy resin. These four mechanical properties were predicted using a model trained with a relatively small amount of experimentally gathered data, and through a series of error analysis the accuracy and future potential of the model was validated.

The models developed in these and other prominent studies of similar nature encompass a variety of ML algorithms, dataset collection methods, and applicable structure-material combinations (Table 1). However, there is currently a lack of models that have the capability of making predictions for datasets containing a wide variety of both structural geometry and base material. Specifically, most ML models that predict the mechanical performance of 3D printed structures tend to be created for a range of geometries, but only a specific material or composite of two specific materials [46.47]. Due to the complexity of material-geometry interactions. further model development and evaluation is necessary for models that incorporate variations in both material and structure geometry. Additionally, models trained and evaluated using solely numerical simulation data may not be reliable for making predictions of 3D printed structures due to the potential impacts of post-processing and printing defects on the geometric accuracy and mechanical performance of these structures [57-60]. Thus, incorporation of experimentally gathered data for model training and evaluation is crucial when working with 3D printed structures. Furthermore, both experimental and numerical collection of 3D printed structure mechanical performance datasets can be time consuming and costly. To obtain this data experimentally, samples must be fabricated and physically tested, often with expensive equipment and materials. Using numerical simulation to gather the data from geometrically complex lattice structures requires significant computational power that can increase both the time and cost of the data collection. Consequently, the large dataset size commonly required to sufficiently train deep learning models like neural networks promotes investigation of simpler models such as kernel regression or support vector machines for making predictions of 3D printed structure mechanical performance.

The overarching purpose of this work was to demonstrate the potential of a simple ML model and limited dataset size in making mechanical performance predictions of 3D printed structures constructed from a wide range of both structural porosity *and* base material. Kernel ridge regression (KRR) and experimentally gathered data were used to develop a ML model capable of predicting

Table 1Examples of current ML models that are used to predict mechanical properties of lattice or composite structures using a range of geometries or materials.

Ref.	ML algorithm	Data collection	Dataset size	Geometry/Material	Model prediction
[21]	ANN	Exp.	15	LPBF printed diamond lattice/Ti6Al4V	Strength, stiffness
[48]	3DCNN & RNN	FEA	100,000	Solid/annealed austenitic stainless steel	Stress-strain curve
[49]	2DCNN w/ PCA	FEA	729	3D aorta models/aorta tissue	Entire stress response field
[51]	3DCNN	CGMD	480	Phase-separated copolymer/an elastomer	Stress-strain curve
[52]	2DCNN	FEA	35,960	2D porous grid/graphene	Shear toughness
[53]	GAN	FEA	2000	2D composite grid/1 brittle & 1 soft material	Entire stress response field
[54]	2DCNN	FEA & Exp.	100.000	2D composite grid/Stratasys Vero & Tango+	Entire stress response field
[55]	2DCNN w/ PCA	FEA	100,000	2D composite grid/1 brittle & 1 soft material	Stress-strain curve
[56]	ANN	Exp.	160	Reinforced tube/epoxy resin & carbon fiber	Force, displacement
[79]	2DCNN	FEA & Exp.	1600	LPBF printed lattice/AlSi10Mg	Stress-strain curve

Young's modulus, yield strength, fracture strength, and fracture strain of periodic gyroid lattice structures manufactured using vat photopolymerization (VPP) 3D printing. The gyroid structure was selected among other TPMS and strut-based topologies due to its demonstrated mechanical performance and proven versatility in multiple fields and applications [19,24,25,61-63]. Utilization of a simple algorithm like KRR allowed for creation of a ML model that is easily interpreted, easily modifiable, and capable of producing accurate predictions from training on a relatively small dataset. This reduces the cost and time required to generate the training dataset, as fewer printed samples are needed for physical testing and less simulations are needed for numerical simulation. By choosing to gather a small set of high-quality experimental data for training the model, we can effectively analyze and capture the effects of post-processing and printing defects and use these observations to inform future model development.

We first describe the scope of the dataset and the data collection methods used. The framework of the ML model and the model training process are then presented, followed by simulation parameters used to gather FEA data for comparing to the model's predictions. Finally, model performance results are presented and discussed.

2. Materials and methods

2.1. Material dataset curation

Mechanical properties of commercially available photopolymer materials were reviewed and compiled into a database. The mechanical properties published by the manufacturers of these 3D printing resins were plotted on Ashby plots to create relative comparisons and visualize the spectrum of currently available materials (Fig. 1). Out of 197 total materials in the database, sixteen were selected to be used for training the ML model (hereafter referred to as the "training set" of materials) and four were selected to be used for evaluating the performance of the final, fully trained model (hereafter referred to as the "evaluation set" of materials). For material selection rationale and to understand why evaluation set materials were picked to be the upper-right most materials on Fig. 1, see Section 4.1. The brand names of the sixteen materials in the training set and the four materials in the evaluation set have been replaced by M1-M16 and M17-M20, respectively, throughout the remainder of this paper for simplification (Fig. 2A, B). For a list matching each M value to the corresponding material, manufacturer, and printer used, see the corresponding Data in Brief article [78].

2.2. Design and fabrication of samples

The samples were printed on three different machines, specifically a Formlabs Form2, ETEC Envision One, and Prusa SL1, due to proprietary printing restrictions of some of the materials in the

dataset. The sample geometry consisted of a cylindrical region of diameter 12 mm and height 17 mm and tabs on top and bottom of the cylinder for interfacing with the grips of the mechanical testing machine, and all samples were printed with their longest dimension orthogonal to the build plate. While the unit cell of a gyroid is cubic, there is an extensive amount of literature where cylindrical samples have been used [3,64-66], and with a D/u value (diameter of the cylinder cross-section divided by unit cell size) greater than or equal to 2, the boundary effects caused by a small number of unit cells within the cylindrical structure are negligible and demonstrate a convergence of mechanical properties such as strength and stiffness for a given porosity [65]. The cylindrical regions were populated with the "Gyroid" triply periodic minimal surface (TPMS) lattice structure with unit cell size of 5x5x5mm and porosity of 55% to 85% in 5% increments (Fig. 2C) altered by changing the wall thickness of the lattice. For all materials M1-M20, three duplicate samples for each of the seven designed porosities were printed, which would create a total of 420 samples. Due to potential aspects of VPP 3D printing and post-processing, such as trapped resin and other defects, there can be discrepancies in measured porosity among duplicate samples of the same designed porosity [43–45] (Fig. 2C). These discrepancies created a spectrum of measured or "as-printed" sample porosity values composed of a unique porosity value for each of the printed samples. Thus, printing three duplicate samples for each of the seven designed porosities resulted in 21 samples of unique measured porosity for each material. This was an unintentional result, but ultimately it created a larger dataset and inspired further analysis that is discussed in Section 4.2. After occasional premature sample failure of some of the fragile, higher-porosity samples during post-processing and mechanical testing, a final count of 314 training set samples and 75 evaluation set samples was achieved. For further details regarding sample design, printing procedure, sample handling, and mechanical testing, see the corresponding Data in Brief article [78].

2.3. Sample porosity measurements

See the corresponding Data in Brief article [78] for the porosity measurement procedure and measured porosity values for all samples.

2.4. Mechanical testing and selecting properties

The stress–strain curve of each sample was recorded using an MTS Criterion C43.504 test machine and following ASTM D638-14 standards and guidelines. For details regarding data collection and conversion of displacement and load data from the test machine to strain and stress data, see the corresponding Data in Brief article [78]. All samples failed within the lattice cylinder region and were tested in tension at a rate of 5 mm/min. The focus of this study was determining the capability of a singular machine learning model in making mechanical performance predictions

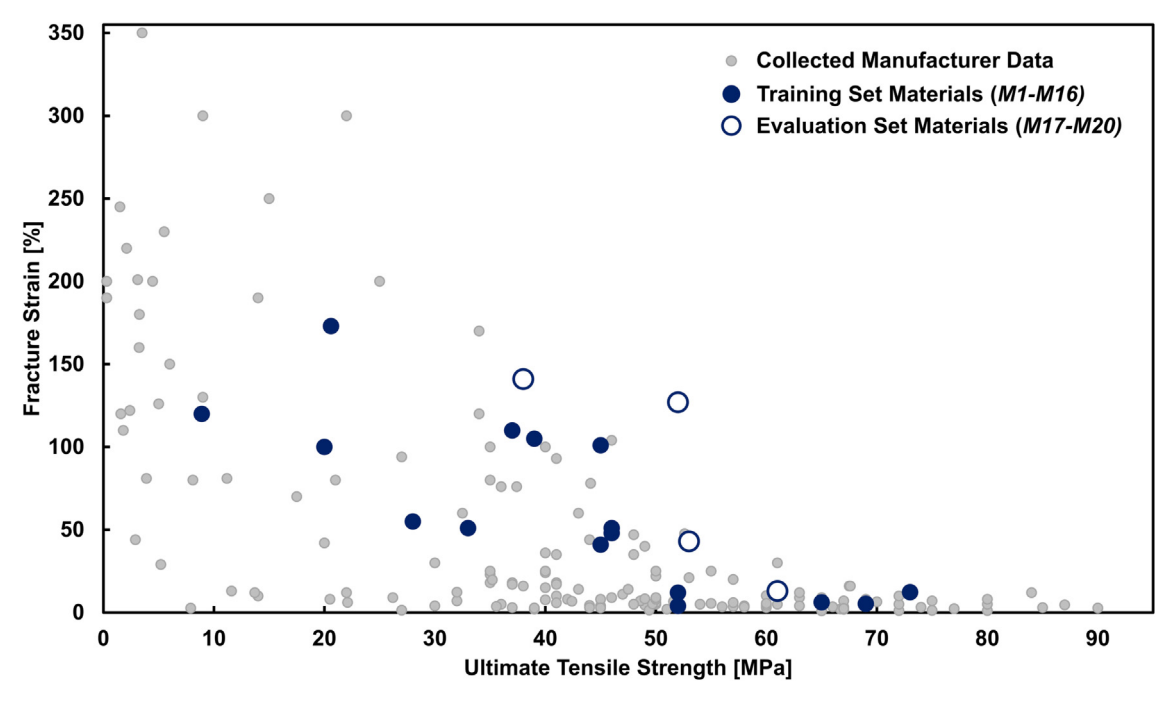


Fig. 1. A plot showing the compiled database of 3D printable photopolymer materials. Larger black and white circles represent materials used in the ML model training set and evaluation set, respectively. The 20 materials selected for this work possess mechanical properties that span a wide range of what is currently available from manufacturers.

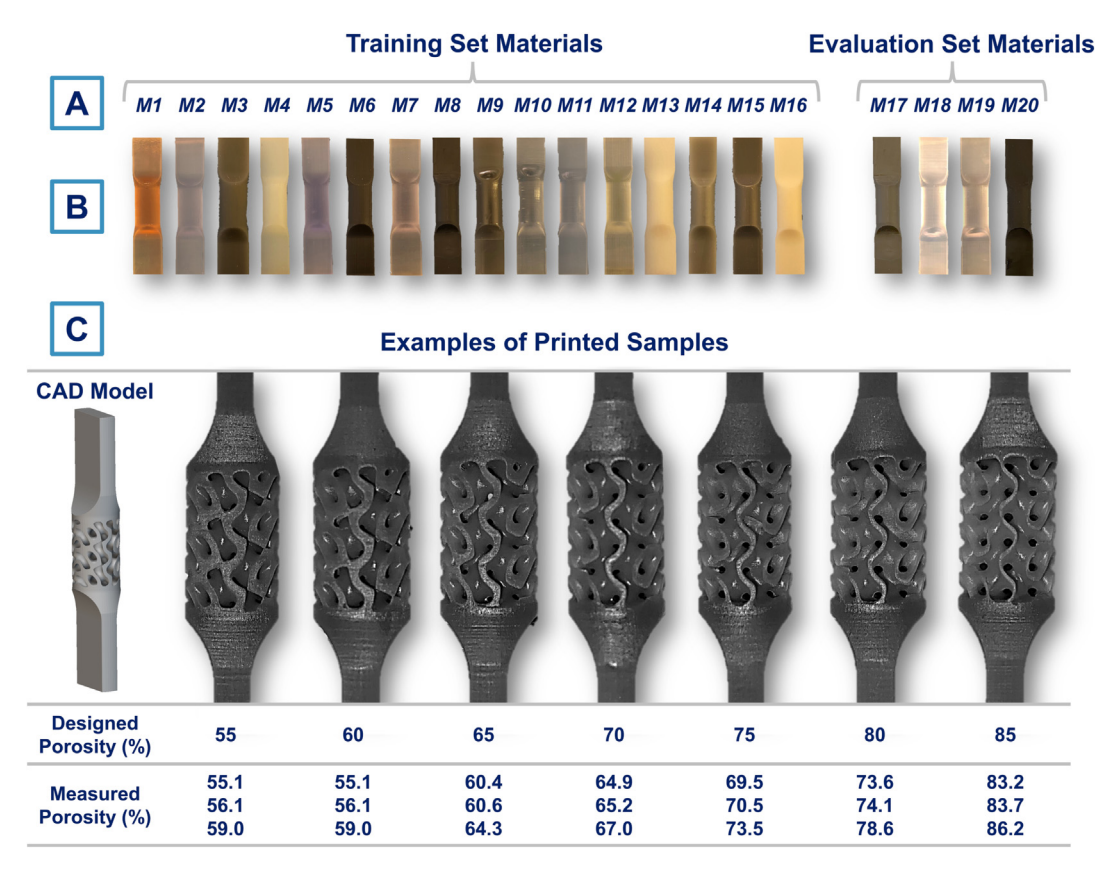


Fig. 2. Visualization of training and evaluation set material groupings and images of printed samples with demonstrated measured vs. designed porosity. (A) The samples printed with each material *M1-M20* are separated into training and evaluation sets. (B) A printed 0% porosity sample for each material is displayed to help with visualization of data separation. (C) Examples of printed lattice structures are shown along with the CAD model of a representative sample. The three duplicate samples each have a unique measured porosity, slightly different from the designed value, and thus are all included in the input dataset as unique samples.

from a range of both porosity and material, and thus the testing method was kept constant by performing solely tensile testing. Tensile testing was selected over compressive testing due to the clearly defined failure point that occurs when pulling a sample in tension. A custom MATLAB script (see the corresponding Data in Brief article [78]) was used to import the data from the testing machine and extract mechanical properties from the stress–strain curve. Young's modulus $(E^M(p))$, yield strength $(\sigma_Y^M(p))$, fracture strength $(\sigma_F^M(p))$, and fracture strain $(\epsilon_F^M(p))$ for each material M and measured porosity p were extracted from the stress–strain curves (Fig. 3). These four extracted properties would later be used as targets for training the ML model.

2.5. Training the machine learning model

The open-source scikit-learn Python package was utilized for training and evaluating the ML model. The process of training the model included selecting the type of ML algorithm, identifying the highest-performing kernel for this algorithm, and finally, tuning the hyperparameters of the model to achieve higher predictive performance. As mentioned in Section 1, KRR was selected as the algorithm for training the model due to its ability to reduce overfitting, kernelize data for performing higher-dimensional regression, and provide an interpretable way to solve non-linear problems by relying on a relatively simple framework and minimization strategy. The model uses measured sample porosity p and manufacturer-published mechanical properties of the material M to predict the mechanical property targets of a lattice structure with the given porosity p and printed out of the given material M(Fig. 4). The ranges for the input and output parameters of the model are listed in Table 2.

Using KRR for training the ML model involved attempting to minimize the loss function:

$$F(\lambda) = \|\mathbf{Y} - \mathbf{X}\lambda\|_2^2 + \mathbf{C}\|\lambda\|_2^2 \tag{1}$$

where X are the inputs or features, Y are the outputs or targets, λ are the weights to be applied to features, C is the regularization strength, and $F(\lambda)$ is the loss function to be minimized. The loss function in Eq. (1) is further manipulated to allow for kernelization of the input data by creating a matrix of inner products to get the final loss function:

$$F(r) = ||Y - Kr||_2^2 + C\langle r, Kr\rangle$$
 (2)

where **K** is the specific kernel operator used and $\lambda = Xr$.

The feature and target arrays compiled using the MATLAB script noted in Section 2.4 were imported into a Python script to utilize the scikit-learn package. A grid search was coupled with cross-validation (CV) to determine the highest-performing kernel. The folds used for CV were created using a "leave one out" method to reduce overfitting of the model, where each fold corresponded to the set of samples printed from one of the materials. All models created in the grid search were fitted using the current training fold and evaluated for performance on the current validation set. The Laplacian kernel proved to be the highest-performing kernel on average. The performance of each generated model was determined using the square of the regression coefficient (\mathbf{R}^2) defined in Section 2.7.

After selecting the Laplacian kernel, a more exhaustive hyperparameter grid search was created to finely tune the hyperparameters. The Laplacian kernel has the form:

$$K(X_1, X_2) = e^{\gamma ||X_1 - X_2||_1}$$
(3)

which has as a tunable hyperparameter only gamma (γ) . Inserting the Laplacian kernel of Eq. (3) into Eq. (2), we see that the tunable hyperparameters for this model are alpha (C in Eq. 2) and gamma. To optimize the alpha and gamma hyperparameters, the second grid search was performed, now with a fixed Laplacian kernel and larger set of values for each hyperparameter. Ultimately, an alpha value of 0.0092 and gamma value of 0.001 created the highest-performing model and were used in the final model training.

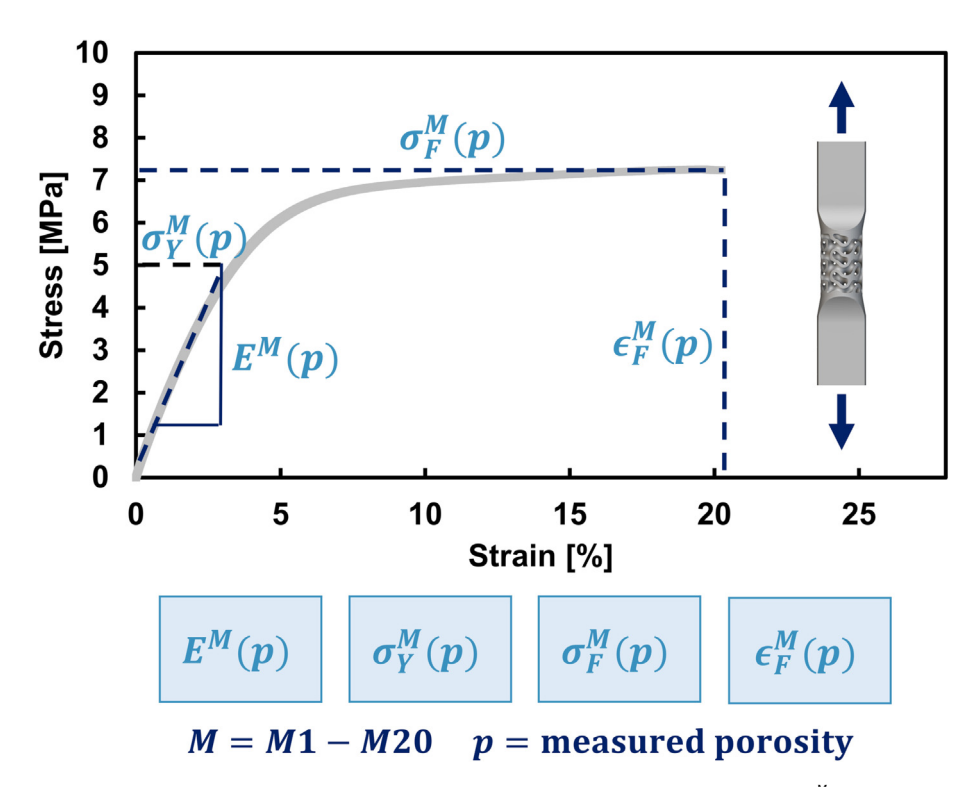


Fig. 3. Diagram showing the process of extracting properties from stress-strain curves. For each sample, Young's Modulus $(E^{\mathbb{M}}(p))$, yield strength $(\sigma_{Y}^{\mathbb{M}}(p))$, fracture strength $(\sigma_{F}^{\mathbb{M}}(p))$, and fracture strain $(\epsilon_{F}^{\mathbb{M}}(p))$ are extracted and used as targets for the ML model.

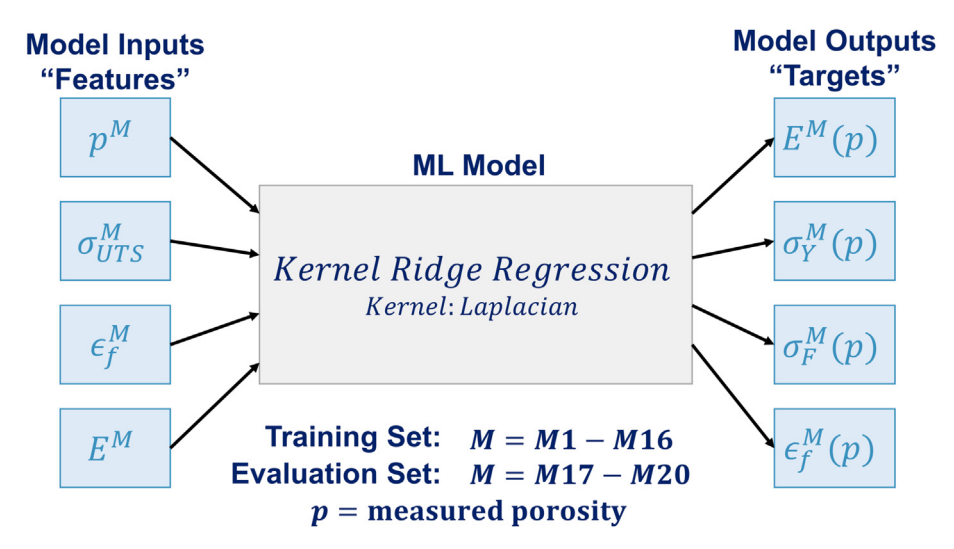


Fig. 4. Visualization of what the ML model accepts as input features and is trained to produce as output. During model training, measured porosities p and published mechanical properties for all materials M are used as input. The corresponding output targets are the lattice structure mechanical properties extracted from a sample printed with the input material M and porosity p. For example, E^M is read as "the ultimate strength of material M" and p^M is read as "the porosity p assigned to material M", while $E^M(p)$ is read as "the Young's modulus for a lattice sample of porosity p printed using material M".

Table 2Units and range of data for each input and output parameter of the ML model.

Input parameter "Feature"	Unit	Data range	Output parameter "Target"	Unit	Data range
Porosity (p)	%	23.1-92.6	Young's modulus of printed structure $(E^M(p))$	MPa	0.32-408.89
Young's modulus of material (E^M)	MPa	4.6-4100	Yield strength of printed structure $(\sigma_Y^M(p))$	MPa	0.11-14.31
Ultimate strength of material (σ_{IJIS}^{M})	MPa	8.9-73	Fracture strength of printed structure $(\sigma_F^M(p))$	MPa	0.14-15.75
Fracture strain of material (ϵ_F^M)	%	4-173	Fracture strain of printed structure $(\epsilon_F^M(p))$	%	1.38-121.95

After fully training the model, samples from the evaluation set of materials *M17-M20* were used to evaluate the model's performance. The features of the evaluation set materials were input into the model, and the model's predictions of mechanical properties for the input material and porosity were compared to the experimentally gathered target values. Evaluation metrics are listed in Section 2.7, and the accuracy and overall performance of the model is presented in Sections 3.2 and 3.3.

2.6. Finite element analysis (FEA)

The CAD designs for evaluation set material samples with 55, 70, and 85 % porosity values were used for FEA simulation, creating 12 simulations in total. The selected samples span all the evaluation set materials and the lowest, middle, and highest porosity values. The accuracy of ML model predictions was validated against experimental results, so these simulations were used solely to compare the speed of FEA simulations to ML model predictions. Simulations were carried out using the Abaqus software suite from Dassault Systèmes. Abaqus/Standard was chosen over Abaqus/ Explicit due to the relatively slow test rate used in earlier physical testing, as described in Section 2.4, and the resulting lack of highspeed dynamic events. Due to the geometric complexity of the designs and the challenges of FEA modeling for plastic deformation, the simulation was run only until a total displacement of 2 mm or approximately 8% strain (Fig. 5C). After the tensile tests were simulated, output data from the simulation was converted into a readable stress-strain curve using a custom script written for Abaqus, and Young's modulus and yield strength were extracted using the MATLAB script mentioned in Section 2.4. For more details regarding FEA parameters, computational resources, and setup, see the corresponding Data in Brief article [78].

2.7. Model evaluation metrics

Various evaluation metrics were used in hyperparameter optimization and performance evaluation. Optimization of hyperparameters during model training was completed using the square of the regression coefficient (\mathbf{R}^2) to compare model performance:

$$\mathbf{R}^{2} = 1 - \frac{\sum_{i=1}^{N} (\mathbf{y}_{i} - \mathbf{p}_{i})^{2}}{\sum_{i=1}^{N} (\mathbf{y}_{i} - \bar{\mathbf{y}})^{2}}$$
(4)

where N is the number of samples, y is a vector of target values, y is the average of all target values, p is a vector of the corresponding predicted values, and a value of R^2 closer to 1 indicates a higher degree of accuracy. Additionally, the root mean squared error (RMSE) and mean absolute percentage error (MAPE) were used with R^2 to make further quantifications and analysis of model performance using the evaluation set:

$$RMSE = \sqrt{\frac{\sum\limits_{i=1}^{N} (y_i - p_i)^2}{N}}$$
 (5)

$$MAPE = \frac{1}{N} * \sum_{i=1}^{N} \frac{(\mathbf{y}_i - \mathbf{p}_i)^2}{\mathbf{y}_i}$$
 (6)

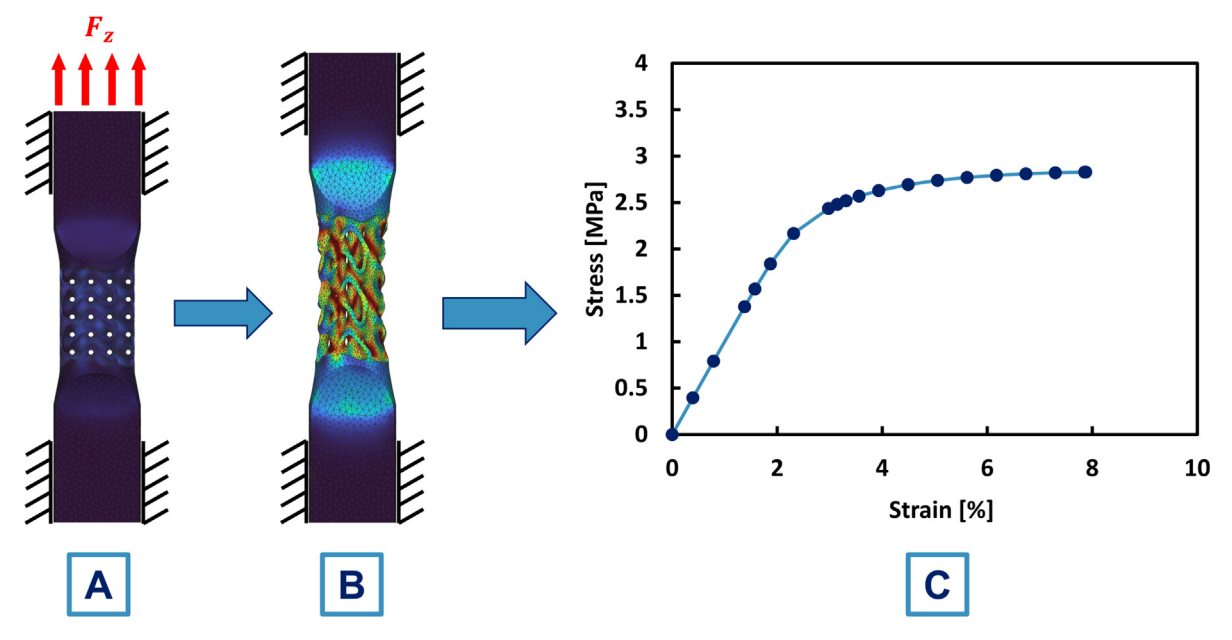


Fig. 5. Visualization of FEA simulation process. (A) 3D computer model of the sample is restrained and subjected to an applied axial force F_Z . (B) The result of the applied force is simulated and displayed with a colormap to indicate stress levels. (C) A custom script is used to extract the stress–strain curve from the Abaqus FEA simulation.

3. Results

3.1. Measured lattice structure porosity

Although the designed porosity range of 55% to 85% was consistent for all evaluation materials, the measured porosity of samples varied from material to material (Fig. 6). Materials *M18* and *M19* produced printed structures with porosity as low as approximately 25%, far exceeding the lowest of the designed porosities of 55%. Material *M17* produced samples with measured porosity in the range of 45% to 80%, while material *M20* produced porosity in the range of 60% to 88%. It is apparent that the measured porosity of the samples is not consistently greater or less than the designed porosity, but instead varies from material to material. Causes and consequences of this observation are discussed in Section 4.2.

3.2. Mechanical property predictions

The mechanical property predictions made by the model were separated by evaluation material and mechanical property to gain a qualitative understanding of model performance for each evaluation set material M17-M20 (Fig. 6). For a quantitative analysis, see Section 3.3. The predictions for modulus and strength values followed the experimental values with a decrease in magnitude as porosity increases, as expected [43,44,61], and with a high degree of accuracy. Predictions for fracture strain appeared to be less accurate, and it is apparent from the plots in Fig. 6 that the experimentally gathered values have a higher degree of stochasticity than the other predicted properties. Interestingly, by adding the values of the three most similar materials from the training set relative to each evaluation material and creating a moving average of the added values across porosity, the nature of the fracture strain predictions became apparent. For each evaluation set material, these three most similar materials were referred to as "nearest neighbors" (NNBs), and they represented the materials with mechanical properties most similar to the specific evaluation set materials. KRR works by creating a weighted average of the outputs of NNBs, and therefore it was logical that the predictions would approximately follow these weighted averages represented by the gray dashed lines in each plot (Fig. 6).

3.3. Model performance

Model performance was evaluated quantitatively with R^2 , RMSE, and MAPE (Table 3) using Equations (4), 5, and 6, respectively. The model performed best at predicting Young's modulus of the samples, achieving an R^2 of 0.956. The model performed similarly when predicting yield strength and fracture strength values of the samples. R^2 of 0.875 and 0.871 were achieved when predicting yield strength and fracture strength, respectively. The model did not perform as well when predicting fracture strain, achieving an R^2 of 0.505. By examining the RMSE and MAPE, the significance of this difference in R^2 can be realized by the large error of 43.0% for fracture strain. The model performed quite well using the training set, achieving an average R^2 of 0.970. A high training accuracy compared to a lower evaluation accuracy indicated that the model may have been overfitted.

Further investigation of model performance was conducted by analyzing the correlation plots for each predicted property. The predictions for modulus and strength showed a symmetric distribution of data about the fitted trendline (Fig. 7A–C), indicating that the model did not consistently predict values higher or lower than the experimental values. For fracture strain (Fig. 7D), the model consistently underpredicted for samples with fracture strain lower than 20%, and then overpredicted for those with fracture strain higher than 20%. This sudden change in the relation between experimental and predicted fracture strain indicates that there is a threshold where the model begins to change from underpredicting to overpredicting values of fracture strain, and potential causes are discussed in Section 4.2.

3.4. Feature importance

The dependency of each of the four predicted properties on the four inputs was determined by computing the model reliance ratio (*MRR*) of each input feature:

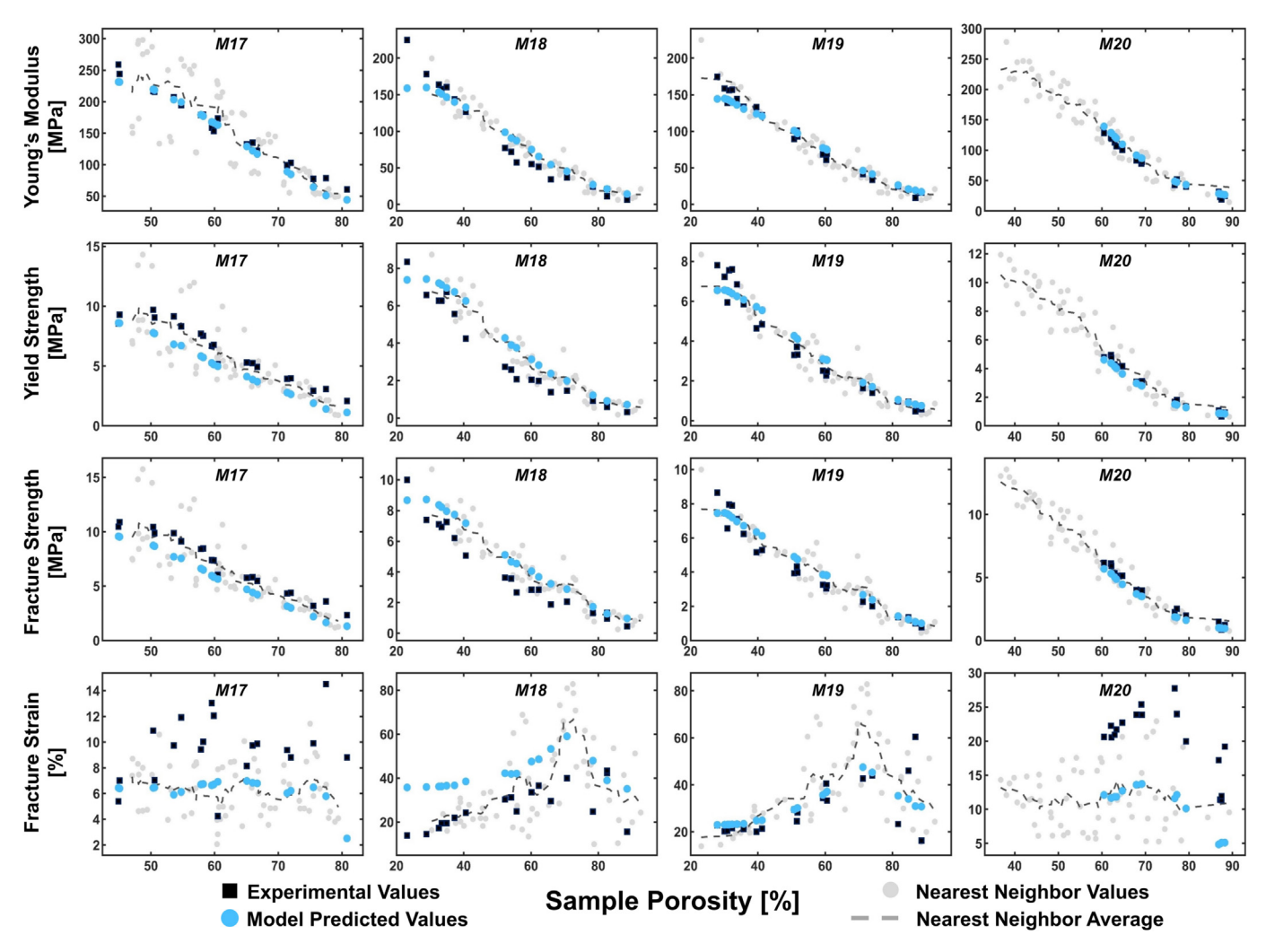


Fig. 6. Plots of predicted and experimentally measured mechanical properties vs. measured sample porosity. Plots are organized in columns by evaluation set material (*M17-M20*), and in rows by mechanical property. Gray dots represent the measured lattice structure mechanical properties of the NNB from the set *M1-M16* to the given evaluation set material *M17*, *M18*, *M19*, or *M20*. The gray dashed line represents a moving average of the mechanical property measurements for the NNB predictions.

Table 3ML model performance of all four target parameters for both the training and evaluation dataset. The metrics presented are root mean squared error (*RMSE*), mean absolute percentage error (*MAPE*), and square of the correlational coefficient (R^2).

Predicted parameter "Target"	Dataset	RMSE	MAPE	R^2
Young's modulus $(E^M(p))$	Train	10.666	16.0%	0.982
(u//	Evaluation	13.962	26.3%	0.956
Yield strength $(\sigma_v^M(p))$	Train	0.509	13.5%	0.969
0 (147)	Evaluation	0.958	23.5%	0.875
Fracture strength $(\sigma_F^M(p))$	Train	0.524	10.0%	0.971
S (F 4 //	Evaluation	1.021	21.5%	0.871
Fracture strain $(\epsilon_F^M(p))$	Train	4.893	15.8%	0.963
(1, (1))	Evaluation	10.862	43.0%	0.505

$$MRR = \frac{MSE_{scrambled}}{MSE_{normal}} = \frac{\sqrt{RMSE_{scrambled}}}{\sqrt{RMSE}} \tag{7}$$

by randomizing the distribution of one of the input features and comparing the calculated **RMSE** of the predictions with "scrambled" inputs to the original **RMSE**. The **MRR** values for each input feature were normalized and compared graphically (Fig. 8). Predicted properties showed a heavy reliance on the porosity of the structure and the Young's modulus of the base material.

3.5. FEA results

Quantification of the FEA simulation performance was made using RMSE and R^2 and compared to the performance of the ML model predictions using the 12 samples described in Section 2.6. The FEA simulation performed slightly better when predicting Young's modulus, with an increase in R^2 of 0.02 but performed with a larger 0.11 increase over the ML model R^2 for yield strength

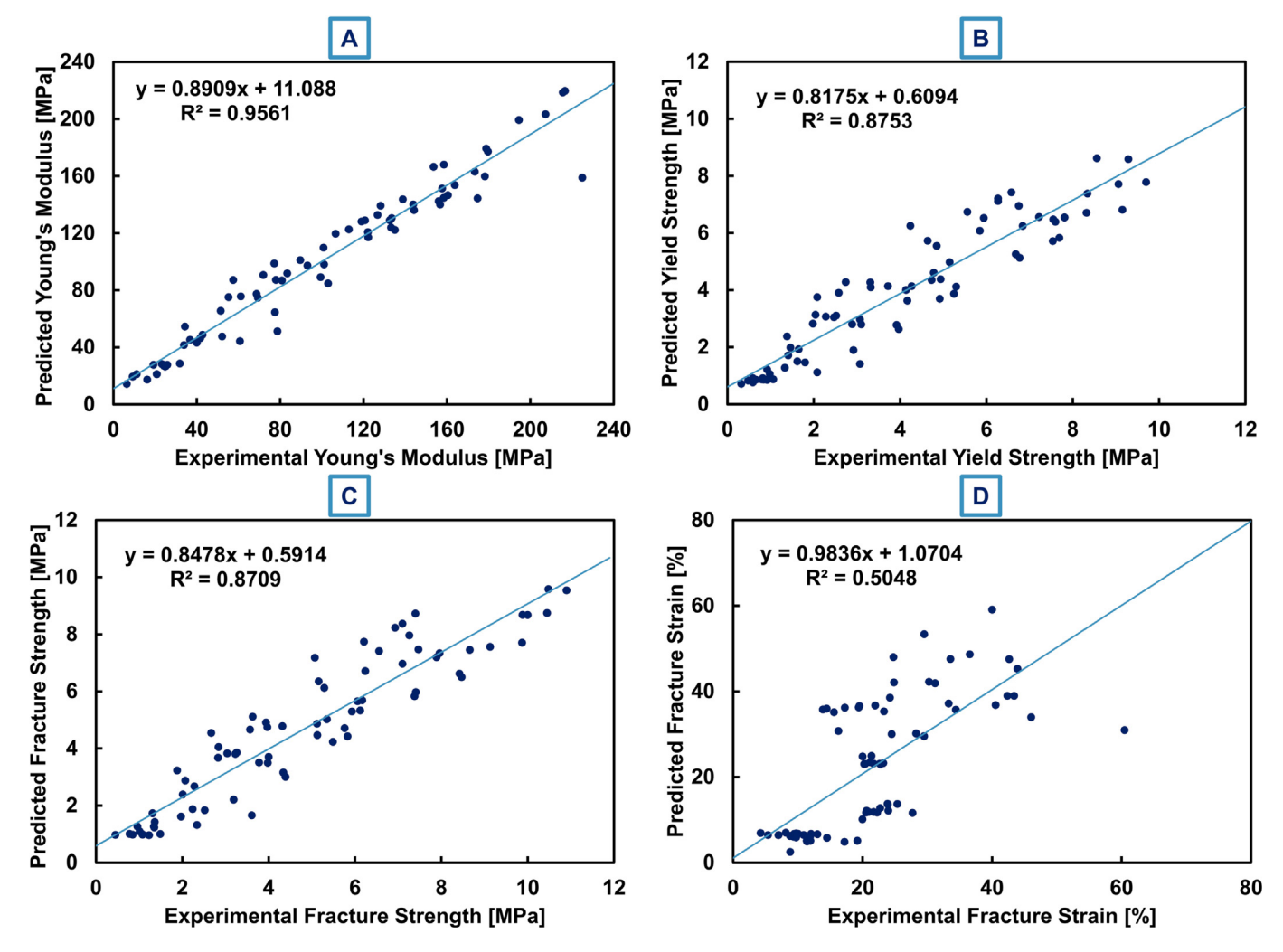


Fig. 7. Model performance plots for all model predictions, separated by predicted property. On each plot, model predictions for the mechanical properties are plotted on the vertical axis and the corresponding experimentally measured values are plotted on the horizontal axis. The mechanical property for each plot is identified by label: (A) Young's modulus, (B) yield strength, (C) fracture strength, (D) fracture strain.

(Table 4). However, the setup time and average time per sample prediction was drastically less when using the ML model. The ML model, once trained, can make predictions almost instantaneously, while the FEA simulation requires meshing and approximately 25 min for each prediction.

4. Discussion

4.1. Choice of print method and materials

Vat photopolymerization 3D printing was selected for creating the dataset due to the growing popularity and increasing number of available materials for this method. Additionally, the wide range of achievable mechanical properties for this class of 3D printable polymers makes VPP a compelling candidate for application of predictive ML models that can predict mechanical properties of 3D printed lattice structures (Fig. 1). Materials M1-M20 were selected from the database of photopolymer materials presented in Section 2.1 based on material availability and the diversity of the mechanical properties of the available materials. In Fig. 1, materials with properties closest to the upper-right corner provide the most favorable combinations of strength and ductility compared to materials in the lower-left corner, which are both weak and brit-

tle. In solid mechanics and across many engineering disciplines, strength and ductility are desired mechanical properties because they give the material the ability to resist deformation in general but also to deform plastically when deformation does occur [67,68]. Out of the 20 materials selected for this study, the four evaluation set materials *M17-M20* were strategically picked to lie outside of the bounds created by the training set materials and closer to this optimal upper-right corner. Thus, successful results using these materials would demonstrate the model's ability to make predictions for materials slightly outside the training set that may contain more desirable mechanical property combinations.

Further investigation into this observation was conducted by making predictions for structures composed of polyetheretherketone "PEEK", a popular high-performance thermoplastic material used in a variety of applications, and two theoretical "digital" materials DM1 and DM2. All three of these materials contained mechanical properties closer to the upper-right corner of Fig. 1, creating combinations beyond those used in the evaluation set (Table 5). Although samples were not printed and physically tested for these materials, providing no way to assess accuracy of model predictions, the model predictions provide further insight into the effect of NNBs. In general, the model predictions for PEEK were similar to *M17*, and the predictions for DM1 and DM2 were similar to *M18* and *M19* (Figs. 6, 9). An interesting behavior occurred for

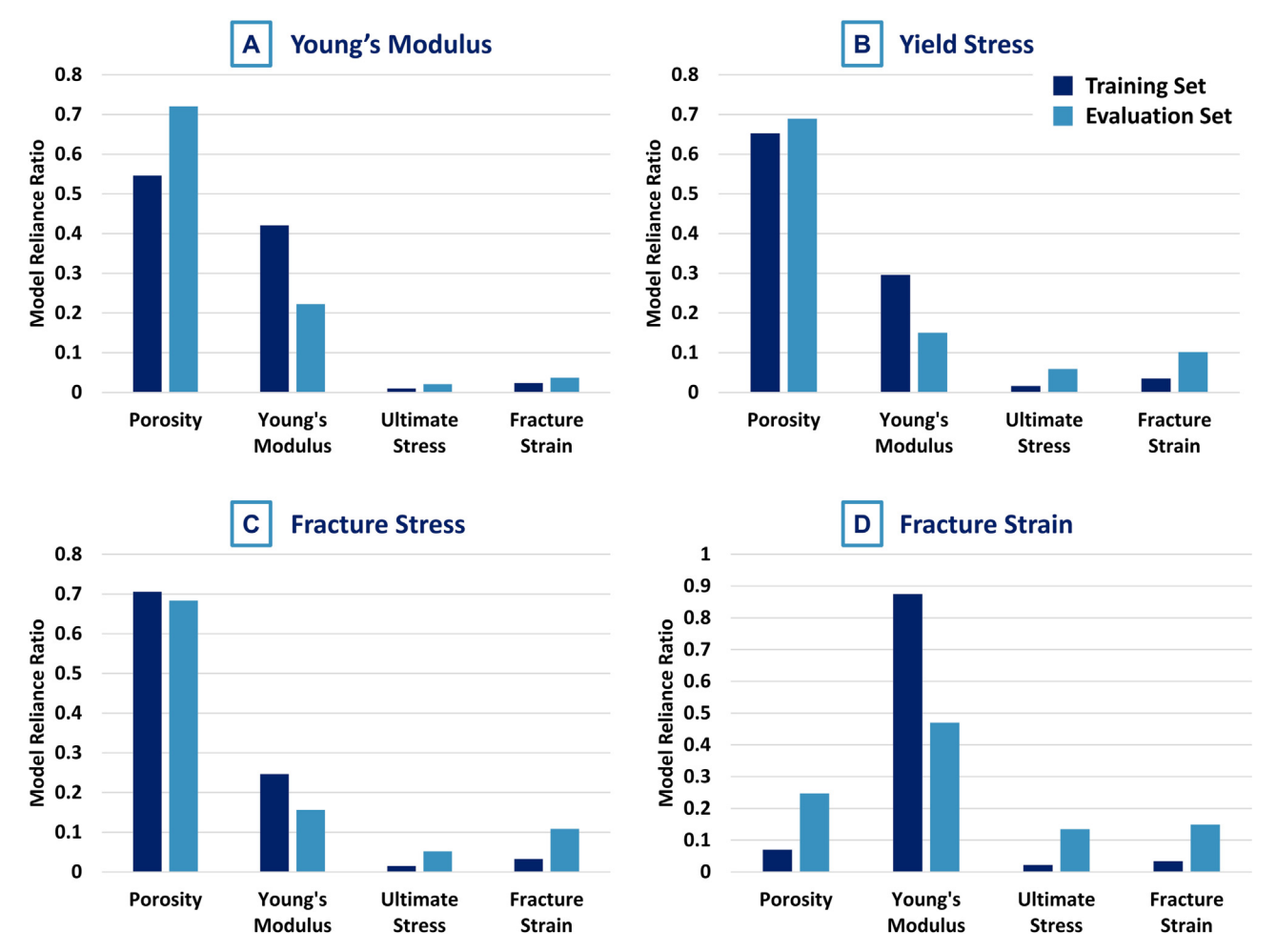


Fig. 8. Model reliance ratio (MRR) for each predicted property and input feature. The plots demonstrate the degree to which each input feature (Young's modulus, ultimate stress, and fracture strain of the base material, and porosity) affects predictions of (A) Young's modulus, (B) yield stress, (C) fracture stress, and (D) fracture strain.

Table 4The predictive performance of the ML model vs. FEA for Young's modulus and yield strength. Model setup time and average time to predict each sample are included.

Method	Young's Modulus		Yield Stress		Setup Time	Setup Time Average Time per Sample	
	R^2	RMSE	R^2	RMSE	[min]	[min]	
KRR Prediction FEA Simulation	0.91 0.93	17.32 26.15	0.77 0.88	0.93 0.79	97 326	4.22e-6 24.8	

Table 5Material property input values for materials PEEK, DM1, and DM2.

Material	Young's Modulus [MPa]	Ultimate Tensile Strength [MPa]	Fracture Strain [%]
PEEK	2900	90	25
DM1	1250	50	200
DM2	1600	60	150

fracture strain predictions of materials DM1 and DM2, where the predicted fracture strain values are steadily increasing between 20% and 70% porosity, but then begin to decrease rather rapidly (Fig. 9). Materials DM1 and DM2 had base material properties that were most similar to materials *M18* and *M19*, and it can be seen by the shape of the moving average NNB prediction dotted line in Fig. 6 that the same NNB samples of M18 and M19 are likely affecting fracture strain predictions for DM1 and DM2. However, while these similarities in fracture strain predictions exist, the effect of

altering the base material property inputs is evident. The higher predicted modulus and strength values for PEEK and DM2 compared to M17 and M18/M19, respectively, demonstrate how, for example, an increase in the Young's modulus and ultimate strength of the base material will change the weighting of the NNBs and produce logical predictions. Thus, adding more data to the training dataset over time will gradually increase the accuracy of model predictions for materials closer to the upper-right corner of the plot in Fig. 1.

Overall, the accuracy of model predictions for the evaluation set (Fig. 7) coupled with the logical influence of NNBs on the PEEK and DM predictions present a compelling case for the use of ML algorithms such as KRR for training models that can predict property outputs of structures with a wide range of materials and geometries. The model can be trained with additional photopolymer materials to increase model performance, and the results show promise for creating similar models for other TPMS topologies such as P and D shell lattices or ultimately developing a single model

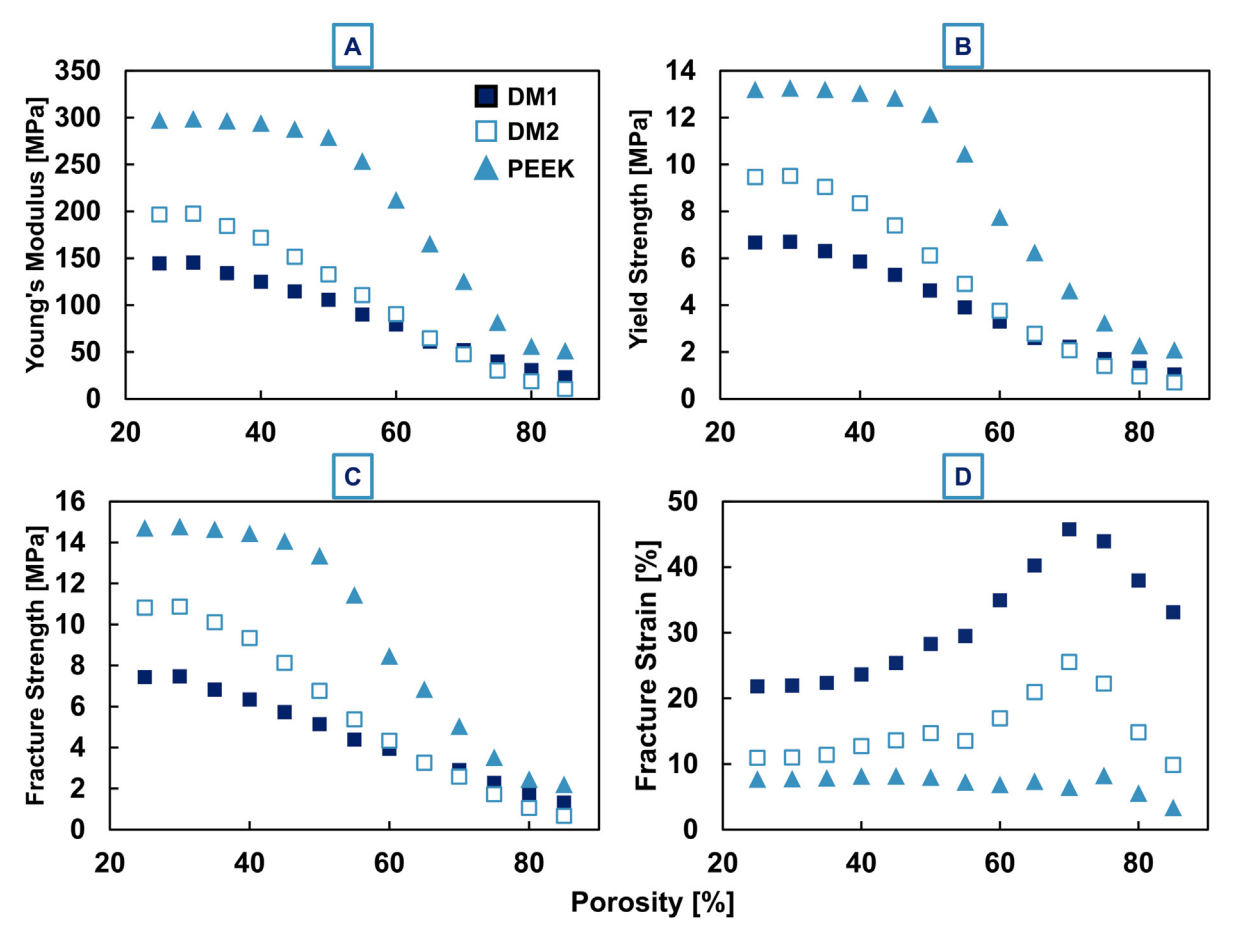


Fig. 9. Plots of the predicted mechanical properties vs. theoretical sample porosity for added materials PEEK, DM1, and DM2.

capable of making predictions for multiple TPMS topologies and porosities.

4.2. Measured lattice structure parameters

When working with complex additive manufacturing processes and geometries, training a ML model with experimental data, or using it to verify samples from numerical simulation, is crucial. Analyzing the dataset used in this research, measured porosity varied greatly from designed values, and gyroid lattices made with VPP experienced stochastic fracture strain (Figs. 2 and 6). The implications of this stochastic nature on model performance are discussed further in Section 4.3.

Porosity was chosen as the geometric descriptor of the lattice structure due to its strong correlation with the mechanical properties of a 3D printed part, even among parts of different lattice topology [7]. The designed porosity range for samples in this experiment was 55% to 85% while measured porosity values showed a much wider distribution from 25 to 88% (Fig. 6). This indicated that there was, on average, more material than desired within the structure, which is a finding consistent among published work on printing gyroid and other lattice structures using VPP, with reported error in measured porosity as high as 25% and 39.7% by Vieira Magaldi et al. and Bochove et al., respectively [44,45]. This extraneous material was likely due to either overpolymerization or trapped resin during the green state of the part (Fig. 10). Over-polymerization may have occurred when printing the LOCTITE AM materials (see the corresponding Data in Brief article [78]) on an open-source Prusa SL1 printer, where a cure test was conducted to attempt to identify optimal curing parameters.

At high porosity, print failure is more likely to occur due to thin-walled parts that are fragile when in their green-state. Therefore, the exposure time or intensity for a given material may have been raised to a level necessary that was necessary for successful prints at high porosity, but that also resulted in over-polymerization. Another cause of over-polymerization could have been uncured resin trapped within the lattice structure during the green state of the part. If any uncured resin was not removed during the wash cycle, then it would cure during the post-cure and result in a lower porosity structure than designed.

Although stochastic fracture strain and inaccurate printed porosity negatively affected model performance, identifying the challenges they pose during experimental work was necessary to guide future considerations for similar work and would have been unaccounted for if solely numerical simulation data had been used.

4.3. Model performance and predictions

Fracture strain predictions were the least accurate (Fig. 7), and this inaccuracy was likely caused by any post-processing defects or printing defects present in the structures. These defects can significantly impact the geometry and performance of 3D printed structures, and can occur while the part is printing, during post-processing, or at any point in the manufacturing process. Defects such as trapped resin or over-polymerization of the polymer decrease the measured porosity by adding extraneous material to the structure (Fig. 10). Surface defects like delamination during printing result in stress concentrations within the structure that cause premature and stochastically occurring fracture (Fig. 10). The random variability in defect severity and frequency among

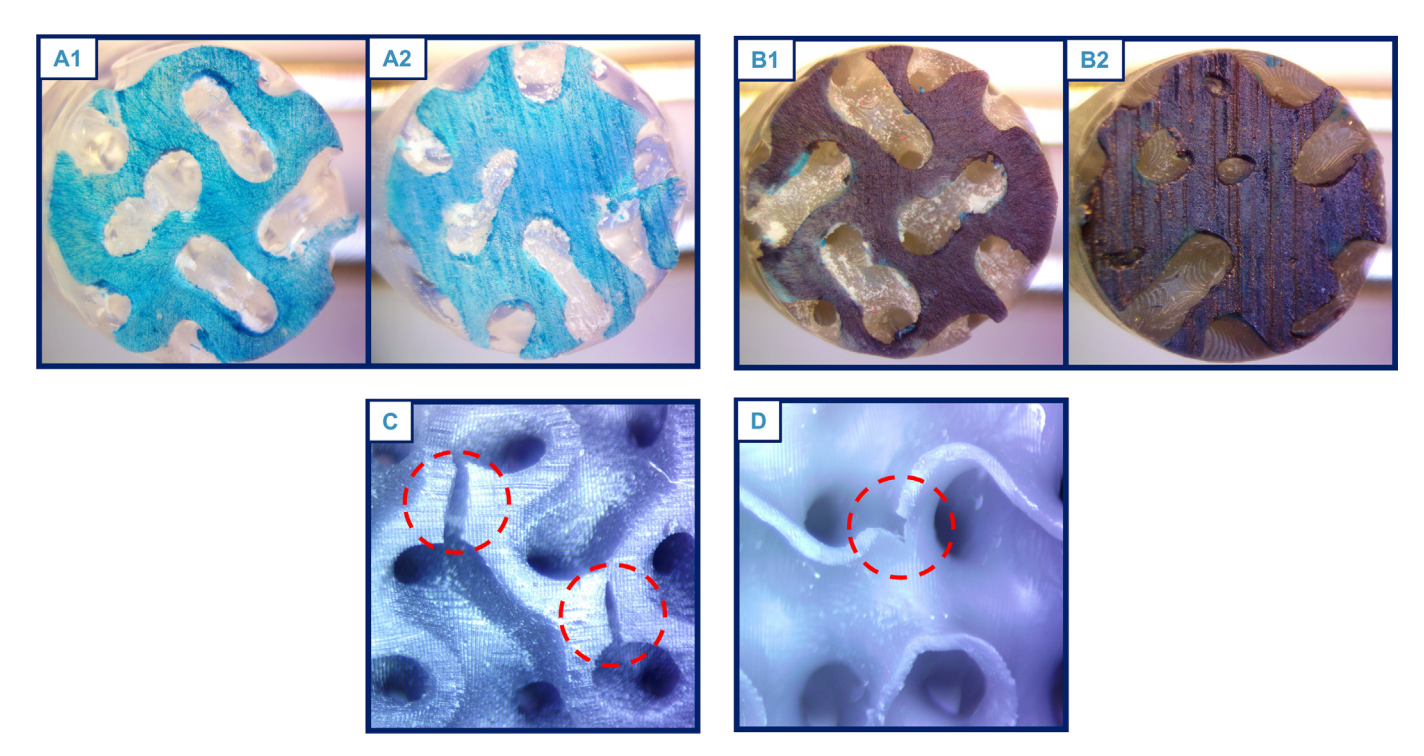


Fig. 10. Microscope images of printed sample defects. Duplicate samples are cut in half and their cross-sections shown side-by-side in (A) and (B), with the cross-sectional surfaces colored blue and black, respectively. The samples in A2 and B2 show extraneous material within the structure that has cured and become solid, changing the measured porosity from the more accurately printed samples A1 and B1, respectively. Close-up images of surface cracks (C) and printing voids (D) highlight potential stress concentrations in structures causing variability in fracture. (For interpretation of the references to colour in this figure legend, the reader is referred to the web version of this article.)

printed parts creates a more stochastic relationship between porosity and fracture strain, which is naturally much more difficult for a ML model to predict. Additionally, due to the porous architecture of lattice structures incremental failure can occur at different locations, and thus two structures with the same number of defects may fail at different locations, and at different times.

Predictions of Young's modulus, yield strength, and fracture strength, with \mathbb{R}^2 values of 0.956, 0.875, and 0.871, respectively, demonstrate a high level of performance. The difference in accuracy for these predicted values versus fracture strain can be explained through examination of an arbitrary stress-strain curve, such as in Fig. 3. All samples failed within the plastic regime at points along the curve to the right of yield. Although fracture strain and fractures stress occur at the same point, the generally low slope of the curve in the plastic regime would cause any premature failure due to surface defects to have a much larger effect on the fracture strain, whose axis is often parallel to the curve in the plastic regime. Consistent failure in the plastic regime also means that yield stress and Young's modulus were relatively unaffected by premature failure, though it should be noted that failure in the linear regime would affect both yield and fracture strength predictions.

Interestingly, predictions for fracture strain were most sensitive to the Young's modulus input, and none of the predicted properties were very sensitive to ultimate strength (Fig. 8). This would suggest that perhaps the modulus of the base material plays a large role in premature fracture of the porous structures. However, it is unlikely that the ultimate strength of the base material would have a low impact on the mechanical performance of these structures, and therefore future model development could include a larger weighting on the less impactful inputs of this study to potentially increase model performance. Additionally, the relatively high error for predicting the fracture strain of evaluation set samples compared to training set samples indicates that the

model may be overfit to the training set (Table 3). This is further suggested by the proximity of fracture strain predictions in the evaluation set materials to the respective moving average of NNB values in the training set (Fig. 6). With a relatively small dataset size for training the model and the impact of NNB values, it is likely that increasing the training set size by adding materials closer in nature to the evaluation set materials would lead to an increase in performance of model predictions for the evaluation set. However, as stated in Section 4.1, one of the goals of this work was to assess the model's predictive ability for materials different in nature, namely with increased strength and ductility, from those used in the training set.

4.4. Comparison to FEA

The similar performance between FEA simulation results and model predictions for Young's modulus and yield strength demonstrates the potential of using ML to expedite the discovery of new structures. The FEA simulation and ML model produced results with similar accuracy for Young's modulus and yield strength (Table 4). This is more impactful when considering the differences in setup time and time per sample prediction. FEA requires a meshing process when using a new geometry and then the simulation itself, while ML can make predictions instantly once trained. For the dataset described in Section 2.6, setup for FEA took three times longer than ML, and the time per sample prediction for ML was a fraction of the $\sim 25~{\rm min}$ FEA simulations.

Once trained, the ML model can make predictions for limitless combinations of photopolymer material and porosity almost instantaneously, and with little computational cost. Additionally, through a cyclic process of new material exploration, experimental validation, and model retraining, the performance of the ML model will continuously improve. Thus, the ML model provides a starting

point for narrowing the search of material and lattice design combinations for a given application.

It has been demonstrated that ML models can make accurate predictions for mechanical properties of various structures using FEA simulation results as the "ground truth" [55,69-71], and extensive work has been done in the field of FEA for simulating the mechanical response of 3D lattice structures [72-77]. Thus, a natural next step is using machine learning to make mechanical property predictions of 3D lattice structures from FEA simulation data considered to be the "ground truth". However, as demonstrated in this work and others [43-45], creation of such lattices using methods like VPP AM can introduce defects and variability that are not well captured by FEA. Thus, utilization of experimental and computational methods for gathering ML model training data coupled with experimental data for validation of performance presents a promising combination for making mechanical property predictions of 3D printed lattice structures in a range of materials and geometries.

4.5. Future work

Future work based on this research includes investigation into surface defects and their impact on 3D printed photopolymer structure fracture strain. Capturing or accounting for the variability of these defects with new or modified input parameters will increase model performance. Additionally, we plan to use the knowledge gained through this investigation to develop a method of identifying how surface defects directly affect or alter the mechanical behavior of these structures, and how this may be incorporated to modify or adjust numerical simulation data to better account for experimental factors. Finally, we will utilize the knowledge gained from this research to extend predictive capabilities to other lattice structures and ultimately other AM methods.

5. Conclusions

Machine learning has been used to predict mechanical properties of 3D printed lattice structures with a range of both geometry and base material properties. Experimentally gathered data was used with a KRR algorithm to develop a simple, interpretable model capable of making accurate predictions for Young's modulus, yield strength, and fracture strength. The predictions of fracture strain were highly sensitive to printing and processing defects within the structures, such as divergence of measured lattice porosity from designed values, and stochastically occurring premature failure of the structures reduced the accuracy of fracture strain predictions. The model was compared directly to FEA simulation and produced results of similar accuracy at a fraction of the time. Nearest neighbor weighting through the KRR training process allows for extension of predictions to include structures with base materials containing favorable mechanical properties that lie outside the domain of the training set.

- A) The model is capable of making predictions using a wide range of materials within the realm of VPP materials, from elastomers to brittle polymers, with high accuracy for predictions of Young's modulus, yield strength, and fracture strength.
- B) The accuracy of model predictions in this study and the strong influence of NNBs present a compelling case for using simple models trained with algorithms like KRR to make predictions of 3D printed lattice structure mechanical properties. Using a relatively small dataset, accurate predictions can be made for a wide range of material and geometry combinations.

- C) Premature fracture, resulting in stochastic distributions of fracture strain for experimentally gathered data, reduces model performance of fracture strain. Identifying causes of premature fracture and accounting for their impact is vital when working with experimental data and should not be ignored when using numerical methods.
- D) Measured porosity can vary drastically from designed values for 3D printed lattice structures manufactured with VPP. Accounting for such differences in geometry is crucial when working with VPP, and similar attention should be paid to geometry when using other AM methods, as well as numerically gathered data, if accurate mechanical property predictions are desired.
- E) As new materials and printing methods are developed, a combination of experimental data, numerical data, and ML methods with relatively few inputs presents a promising method for expediting discovery of structure–material-geo metry relationship of 3D printed lattice structures.

Declaration of Competing Interest

The authors declare that they have no known competing financial interests or personal relationships that could have appeared to influence the work reported in this paper.

Acknowledgements

The authors acknowledge financial support from the National Science Foundation [DGE-2022040] and the National Science Foundation Graduate Research Fellowship Program. The authors also acknowledge support from the NSF aiM-NRT Research Traineeship program and from Elizabeth Mathey at the University of Colorado Denver Smart Materials and Biomechanics (SMAB) Lab for her gracious assistance with the finite element analysis simulations.

Data Availability

The data and code used for this study is available through the Data in Brief article: Tensile Performance Data of 3D Printed Photopolymer Gyroid Lattices [78].

References

- [1] J. Zhang, X. Chen, Y. Sun, J. Yang, R. Chen, Y. Xiong, W. Hou, L. Bai, Design of a biomimetic graded TPMS scaffold with quantitatively adjustable pore size, Mater. Des. 218 (2022) 110665.
- [2] C. Zhang, Z. Jiang, L.i. Zhao, W. Guo, Z. Jiang, X. Li, G. Chen, Mechanical characteristics and deformation mechanism of functionally graded triply periodic minimal surface structures fabricated using stereolithography, Int. J. Mech. Sci. 208 (2021) 106679.
- [3] C. Pan, Y. Han, J. Lu, Design and optimization of lattice structures: a review, Appl. Sci. (Switzerland) 10 (2020) 1–36, https://doi.org/10.3390/APP10186374.
- [4] H.M.A. Kolken, S.J.P. Callens, M.A. Leeflang, M.J. Mirzaali, A.A. Zadpoor, Merging strut-based and minimal surface meta-biomaterials: Decoupling surface area from mechanical properties, Addit. Manuf. 52 (2022) 102684.
- [5] O. Al-Ketan, D.W. Lee, R. Rowshan, R.K. Abu Al-Rub, Functionally graded and multi-morphology sheet TPMS lattices: design, manufacturing, and mechanical properties, J. Mech. Behav. Biomed. Mater. 102 (2020), https:// doi.org/10.1016/j.jmbbm.2019.103520.
- [6] A.M. Abou-Ali, O. Al-Ketan, D.-W. Lee, R. Rowshan, R.K. Abu Al-Rub, Abu Al-Rub, Mechanical behavior of polymeric selective laser sintered ligament and sheet based lattices of triply periodic minimal surface architectures, Mater. Des. 196 (2020) 109100.
- [7] C.N. Kelly, C. Kahra, H.J. Maier, K. Gall, Processing, structure, and properties of additively manufactured titanium scaffolds with gyroid-sheet architecture, Addit. Manuf. 41 (2021) 101916.
- [8] C.N. Kelly, T. Wang, J. Crowley, D. Wills, M.H. Pelletier, E.R. Westrick, S.B. Adams, K. Gall, W.R. Walsh, High-strength, porous additively manufactured

- implants with optimized mechanical osseointegration, Biomaterials 279 (2021) 121206.
- [9] E.B. Joyee, L.u. Lu, Y. Pan, Analysis of mechanical behavior of 3D printed heterogeneous particle-polymer composites, Compos. B Eng. 173 (2019) 106840
- [10] B. Li, J. Fu, J. Feng, C.e. Shang, Z. Lin, Review of heterogeneous material objects modeling in additive manufacturing, Vis. Comput. Ind. Biomed. Art 3 (1) (2020)
- [11] D.H. Ballard, U. Jammalamadaka, K. Tappa, J.A. Weisman, C.J. Boyer, J.S. Alexander, P.K. Woodard, 3D printing of surgical hernia meshes impregnated with contrast agents: in vitro proof of concept with imaging characteristics on computed tomography, 3D Print Med. 4 (2018), https://doi.org/10.1186/s41205-018-0037-4.
- [12] J. Brie, T. Chartier, C. Chaput, C. Delage, B. Pradeau, F. Caire, M.P. Boncoeur, J.J. Moreau, A new custom made bioceramic implant for the repair of large and complex craniofacial bone defects, J. Cranio-Maxillofac. Surg. 41 (2013) 403–407, https://doi.org/10.1016/j.jcms.2012.11.005.
- [13] K. Chuen Wong, 3D-printed patient-specific applications in orthopedics, Orthop. Res. Rev. 8 (2016) 57–66, https://doi.org/10.2147/ORR.S99614.
- [14] L.E. Murr, S.M. Gaytan, E. Martinez, F. Medina, R.B. Wicker, Next generation orthopaedic implants by additive manufacturing using electron beam melting, Int. J. Biomater. 2012 (2012) 1–14.
- [15] J. Parthasarathy, 3D modeling, custom implants and its future perspectives in craniofacial surgery, Ann Maxillofac Surg. 4 (2014) 9, https://doi.org/10.4103/ 2231-0746 133065
- [16] L. Zhu, N. Li, P.R.N. Childs, Light-weighting in aerospace component and system design, Propulsion and Power, Research 7 (2018) 103–119, https://doi. org/10.1016/j.jppr.2018.04.001.
- [17] T. Dixit, E. Al-Hajri, M.C. Paul, P. Nithiarasu, S. Kumar, High performance, microarchitected, compact heat exchanger enabled by 3D printing, Appl. Therm. Eng. 210 (2022) 118339.
- [18] J. Kim, D.J. Yoo, 3D printed compact heat exchangers with mathematically defined core structures, J. Comput. Des. Eng. 7 (2020) 527–550, https://doi.org/ 10.1093/jcde/qwaa032.
- [19] C.N. Kelly, A.T. Miller, S.J. Hollister, R.E. Guldberg, K. Gall, Design and Structure-Function Characterization of 3D Printed Synthetic Porous Biomaterials for Tissue Engineering, Adv. Healthc. Mater. 7 (7) (2018) 1701095.
- [20] J. Song, Q. Tang, Q. Feng, S. Ma, F. Guo, Q. Han, Investigation on the modelling approach for variable-density lattice structures fabricated using selective laser melting, Mater. Des. 212 (2021) 110236.
- [21] H. Hassanin, Y. Alkendi, M. Elsayed, K. Essa, Y. Zweiri, Controlling the Properties of Additively Manufactured Cellular Structures Using Machine Learning Approaches, Adv. Eng. Mater. 22 (3) (2020) 1901338.
- [22] Q. Liu, R. Xu, Y. Zhou, J. Ge, S. Yuan, Y. Long, T. Shi, Metamaterials mapped lightweight structures by principal stress lines and topology optimization: methodology, additive manufacturing, ductile failure and tests, Mater. Des. 212 (2021) 110192.
- [23] C.N. Kelly, J. Francovich, S. Julmi, D. Safranski, R.E. Guldberg, H.J. Maier, K. Gall, Fatigue behavior of As-built selective laser melted titanium scaffolds with sheet-based gyroid microarchitecture for bone tissue engineering, Acta Biomater. 94 (2019) 610–626, https://doi.org/10.1016/j.actbio.2019.05.046.
- [24] O. Al-Ketan, R. Rowshan, R.K. Abu Al-Rub, Topology-mechanical property relationship of 3D printed strut, skeletal, and sheet based periodic metallic cellular materials, Addit. Manuf. 19 (2018) 167–183, https://doi.org/10.1016/j. addma.2017.12.006.
- [25] M. Akbari, A. Mirabolghasemi, M. Bolhassani, A. Akbarzadeh, M. Akbarzadeh, Strut-based cellular to shellular funicular materials, Adv. Funct. Mater. 32 (14) (2022) 2109725.
- [26] C. Sears, E. Mondragon, Z.I. Richards, N. Sears, D. Chimene, E.P. McNeill, C.A. Gregory, A.K. Gaharwar, R. Kaunas, Conditioning of 3D printed nanoengineered ionic-covalent entanglement scaffolds with iP-hMSCs derived matrix, Adv. Healthc. Mater. 9 (15) (2020) 1901580.
- [27] Y. Ding, A.M. Abdullah, M. Dunn, K. Yu, Design of interfaces to promote the bonding strength between dissimilar materials, J. Manuf. Process. 76 (2022) 786–795, https://doi.org/10.1016/j.jmapro.2022.02.060.
- [28] J.W. Choi, R. Wicker, S.H. Lee, K.H. Choi, C.S. Ha, I. Chung, Fabrication of 3D biocompatible/biodegradable micro-scaffolds using dynamic mask projection microstereolithography, J. Mater. Process. Technol. 209 (2009) 5494–5503, https://doi.org/10.1016/j.jmatprotec.2009.05.004.
- [29] R.B. Osman, A.J. van der Veen, D. Huiberts, D. Wismeijer, N. Alharbi, 3D-printing zirconia implants; a dream or a reality? An in-vitro study evaluating the dimensional accuracy, surface topography and mechanical properties of printed zirconia implant and discs, J. Mech. Behav. Biomed. Mater. 75 (2017) 521–528, https://doi.org/10.1016/j.jmbbm.2017.08.018.
- [30] N.T. Evans, C.W. Irvin, D.L. Safranski, K. Gall, Impact of surface porosity and topography on the mechanical behavior of high strength biomedical polymers, J. Mech. Behav. Biomed. Mater. 59 (2016) 459–473, https://doi.org/10.1016/j. jmbbm.2016.02.033.
- [31] C.N. Kelly, A.SP. Lin, K.EH. Leguineche, S. Shekhar, W.R. Walsh, R.E. Guldberg, K. Gall, Functional repair of critically sized femoral defects treated with bioinspired titanium gyroid-sheet scaffolds, J. Mech. Behav. Biomed. Mater. 116 (2021) 104380.
- [32] A. Heimbrook, C. Kelly, K. Gall, Effects of 3D printed surface topography and normal force on implant expulsion, J. Mech. Behav. Biomed. Mater. 130 (2022) 105208.

- [33] C.R. Hassan, Y.-X. Qin, D.E. Komatsu, S.M.Z. Uddin, Utilization of finite element analysis for articular cartilage tissue engineering, Materials 12 (20) (2019) 3331
- [34] M. Alharbi, I. Kong, V.I. Patel, Simulation of uniaxial stress-strain response of 3D-printed polylactic acid by nonlinear finite element analysis, Appl. Adhes. Sci. 8 (2020), https://doi.org/10.1186/s40563-020-00128-1.
- [35] M. Monti, M. Palenzona, F. Fiorino, F. Baudach, A. Onnis, A. Romeo, Design, manufacturing and FEA prediction of the mechanical behavior of a hybridmolded polycarbonate/continuous carbon fiber reinforced composite component, Compos. B Eng. 238 (2022) 109891.
- [36] S. David Müzel, E.P. Bonhin, N.M. Guimarães, E.S. Guidi, Application of the finite element method in the analysis of composite materials: a review, Polymers (Basel). 12 (4) (2020) 818.
- [37] I.A. Ashcroft, A. Mubashar, Numerical approach: Finite element analysis, Handbook of Adhesion Technology: Second Edition. 1–2 (2018) 701–739. https://doi.org/10.1007/978-3-319-55411-2_25/FIGURES/16.
- [38] S. Gao, R. Liu, H. Xin, H. Liang, Y. Wang, J. Jia, The surface characteristics, microstructure and mechanical properties of peek printed by fused deposition modeling with different raster angles, Polymers (Basel). 14 (1) (2022) 77.
- [39] A.R. Torrado Perez, D.A. Roberson, R.B. Wicker, Fracture surface analysis of 3D-printed tensile specimens of novel ABS-based materials, J. Fail. Anal. Prev. 14 (2014) 343–353, https://doi.org/10.1007/s11668-014-9803-9.
- [40] T.J. Hoskins, K.D. Dearn, S.N. Kukureka, Mechanical performance of PEEK produced by additive manufacturing, Polym. Test. 70 (2018) 511–519, https://doi.org/10.1016/j.polymertesting.2018.08.008.
- [41] X. Deng, Z. Zeng, B. Peng, S. Yan, W. Ke, Mechanical properties optimization of poly-ether-ether-ketone via fused deposition modeling, Materials 11 (2) (2018) 216.
- [42] C.N. Kelly, N.T. Evans, C.W. Irvin, S.C. Chapman, K. Gall, D.L. Safranski, The effect of surface topography and porosity on the tensile fatigue of 3D printed Ti-6Al-4V fabricated by selective laser melting, Mater. Sci. Eng. C 98 (2019) 726–736, https://doi.org/10.1016/j.msec.2019.01.024.
- [43] P.F. Egan, N.R. Khatri, M.A. Parab, A.M.E. Arefin, Mechanics of 3D-printed polymer lattices with varied design and processing strategies, Polymers (Basel). 14 (24) (2022) 5515.
- [44] B. van Bochove, G. Hannink, P. Buma, D.W. Grijpma, Preparation of designed poly(trimethylene carbonate) meniscus implants by stereolithography: challenges in stereolithography, Macromol. Biosci. 16 (2016) 1853–1863, https://doi.org/10.1002/mabi.201600290.
- [45] B. Vieira Magaldi, M. de Oliveira da Costa Maia Pinto, R. Thiré, A.C. Araujo, Comparison of the porosity of scaffolds manufactured by two additive manufacturing technologies: SLA and FDM https://hal.science/hal-03226784.
- [46] S. Nasiri, M.R. Khosravani, Machine learning in predicting mechanical behavior of additively manufactured parts, J. Mater. Res. Technol. 14 (2021) 1137–1153, https://doi.org/10.1016/j.jmrt.2021.07.004.
- [47] F.E. Bock, R.C. Aydin, C.J. Cyron, N. Huber, S.R. Kalidindi, B. Klusemann, A review of the application of machine learning and data mining approaches in continuum materials mechanics, Front. Mater. 6 (2019), https://doi.org/ 10.3389/fmats.2019.00110.
- [48] A.L. Frankel, R.E. Jones, C. Alleman, J.A. Templeton, Predicting the mechanical response of oligocrystals with deep learning, Comput. Mater. Sci 169 (2019) 109099.
- [49] L. Liang, M. Liu, C. Martin, W. Sun, A deep learning approach to estimate stress distribution: a fast and accurate surrogate of finite-element analysis, J. R. Soc. Interface 15 (138) (2018) 20170844.
- [50] H. Salmenjoki, M.J. Alava, L. Laurson, Machine learning plastic deformation of crystals, Nat. Commun. 9 (2018), https://doi.org/10.1038/s41467-018-07737-2.
- [51] T. Aoyagi, High-throughput prediction of stress-strain curves of thermoplastic elastomer model block copolymers by combining hierarchical simulation and deep learning, MRS Adv. 6 (2) (2021) 32–36.
- [52] C.-H. Yu, Z. Qin, M.J. Buehler, Artificial intelligence design algorithm for nanocomposites optimized for shear crack resistance, Nano Futures 3 (3) (2019) 035001.
- [53] Z. Yang, C.-H. Yu, M.J. Buehler, Deep learning model to predict complex stress and strain fields in hierarchical composites, Sci. Adv. 7 (2021), https://doi.org/ 10.1126/sciadv.abd7416.
- [54] G.X. Gu, C.T. Chen, D.J. Richmond, M.J. Buehler, Bioinspired hierarchical composite design using machine learning: Simulation, additive manufacturing, and experiment, Mater. Horiz. 5 (2018) 939–945, https://doi. org/10.1039/c8mh00653a.
- [55] C. Yang, Y. Kim, S. Ryu, G.X. Gu, Prediction of composite microstructure stressstrain curves using convolutional neural networks, Mater. Des. 189 (2020) 108509.
- [56] W. Wang, H.e. Wang, J. Zhou, H. Fan, X. Liu, Machine learning prediction of mechanical properties of braided-textile reinforced tubular structures, Mater. Des. 212 (2021) 110181.
- [57] D.J. McGregor, S. Rylowicz, A. Brenzel, D. Baker, C. Wood, D. Pick, H. Deutchman, C. Shao, S. Tawfick, W.P. King, Analyzing part accuracy and sources of variability for additively manufactured lattice parts made on multiple printers, Addit. Manuf. 40 (2021) 101924.
- [58] R. Chand, V.S. Sharma, R. Trehan, M.K. Gupta, M. Sarikaya, Investigating the Dimensional Accuracy and Surface Roughness for 3D Printed Parts Using a Multi-jet Printer, J. Mater. Eng. Perform. 32 (3) (2023) 1145–1159.
- [59] S. Rouf, A. Raina, M. Irfan Ul Haq, N. Naveed, S. Jeganmohan, A. Farzana Kichloo, 3D printed parts and mechanical properties: Influencing parameters,

- sustainability aspects, global market scenario, challenges and applications, Adv. Ind. Eng. Polym. Res. 5 (3) (2022) 143–158.
- [60] S. Singh, M. Singh, C. Prakash, M.K. Gupta, M. Mia, R. Singh, Optimization and reliability analysis to improve surface quality and mechanical characteristics of heat-treated fused filament fabricated parts, Int. J. Adv. Manuf. Technol. 102 (2019) 1521–1536, https://doi.org/10.1007/s00170-018-03276-8.
- [61] K. Nelson, C.N. Kelly, K. Gall, Effect of stress state on the mechanical behavior of 3D printed porous Ti6Al4V scaffolds produced by laser powder bed fusion, Mater. Sci. Eng. B Solid State Mater. Adv. Technol. 286 (2022) 116013.
- [62] H. Barber, C.N. Kelly, K. Nelson, K. Gall, Compressive anisotropy of sheet and strut based porous Ti-6Al-4V scaffolds, J. Mech. Behav. Biomed. Mater. 115 (2021) 104243.
- [63] J.-W. Luo, Li. Chen, T. Min, F. Shan, Q. Kang, WenQuan Tao, Macroscopic transport properties of Gyroid structures based on pore-scale studies: Permeability, diffusivity and thermal conductivity, Int. J. Heat Mass Transf. 146 (2020) 118837.
- [64] S.M. Ahmadi, G. Campoli, S. Amin Yavari, B. Sajadi, R. Wauthle, J. Schrooten, H. Weinans, A.A. Zadpoor, Mechanical behavior of regular open-cell porous biomaterials made of diamond lattice unit cells, J. Mech. Behav. Biomed. Mater. 34 (2014) 106–115, https://doi.org/10.1016/j.jmbbm.2014.02.003.
- [65] A. Pham, C. Kelly, K. Gall, Free boundary effects and representative volume elements in 3D printed Ti-6Al-4V gyroid structures, J. Mater. Res. 35 (2020) 2547–2555, https://doi.org/10.1557/jmr.2020.105.
- [66] R. Rahmani, M. Rosenberg, A. Ivask, L. Kollo, Comparison of mechanical and antibacterial properties of TiO2/ag ceramics and ti6al4v-TiO2/ag composite materials using combined SLM-SPS techniques, Metals (Basel). 9 (8) (2019) 874
- [67] R.B. Figueiredo, T.G. Langdon, Using severe plastic deformation for the processing of advanced engineering materials, Mater. Trans. 50 (7) (2009) 1613–1619.
- [68] E.F. Oleinik O.B. Salamatina S.N. Rudnev S.V. Shenogin Plastic deformation and performance of engineering polymer materials Polym. Adv. Technol. 6 1 1 9.
- [69] Z. Jin, Z. Zhang, K. Demir, G.X. Gu, Machine learning for advanced additive manufacturing, Matter. 3 (2020) 1541–1556, https://doi.org/10.1016/ i.matt.2020.08.023.
- [70] S. Lee, Z. Zhang, G.X. Gu, Generative machine learning algorithm for lattice structures with superior mechanical properties, Mater. Horiz. 9 (2022) 952– 960, https://doi.org/10.1039/d1mh01792f.

- [71] G.X. Gu, C.T. Chen, M.J. Buehler, De novo composite design based on machine learning algorithm, Extreme Mech. Lett. 18 (2018) 19–28, https://doi.org/ 10.1016/j.eml.2017.10.001.
- [72] D. Li, W. Liao, N. Dai, G. Dong, Y. Tang, Y.M. Xie, Optimal design and modeling of gyroid-based functionally graded cellular structures for additive manufacturing, CAD Computer Aided Design. 104 (2018) 87–99, https://doi. org/10.1016/j.cad.2018.06.003.
- [73] D. Ali, S. Sen, Finite element analysis of mechanical behavior, permeability and fluid induced wall shear stress of high porosity scaffolds with gyroid and lattice-based architectures, J. Mech. Behav. Biomed. Mater. 75 (2017) 262–270, https://doi.org/10.1016/j.jmbbm.2017.07.035.
- [74] W. Hu, X. Cao, X. Zhang, Z. Huang, Z. Chen, W. Wu, Li. Xi, Y. Li, D. Fang, Deformation mechanisms and mechanical performances of architected mechanical metamaterials with gyroid topologies: Synchrotron X-ray radiation in-situ compression experiments and 3D image based finite element analysis, Extreme Mech. Lett. 44 (2021) 101229.
- [75] Z. Li, W. Zhai, X. Li, X. Yu, Z. Guo, Z. Wang, Additively manufactured dual-functional metamaterials with customisable mechanical and sound-absorbing properties, Virtual Phys Prototyp. 17 (2022) 864–880, https://doi.org/10.1080/17452759.2022.2085119.
- [76] C. Chua, S.L. Sing, C.K. Chua, Characterisation of in-situ alloyed titanium-tantalum lattice structures by laser powder bed fusion using finite element analysis, Virtual Phys Prototyp. 18 (2023), https://doi.org/10.1080/17452759.2022.2138463.
- [77] Z. Lai, M. Zhao, C.H. Lim, J.W. Chua, Experimental and numerical studies on the acoustic performance of simple cubic structure lattices fabricated by digital light processing, Mater. Sci. Addit. Manuf. 1 (2022). https://doi.org/10.18063/ msam.v1i4.22.
- [78] J. Peloquin, A. Kirillova, E. Mathey, C. Rudin, L.C. Brinson, K. Gall, Tensile Performance Data of 3D Printed Photopolymer Gyroid Lattices, Data in Brief. In Press.
- [79] H. Yang, W. Wang, C. Li, J. Qi, P. Wang, H. Lei, D. Fang, Deep learning-based X-ray computed tomography image reconstruction and prediction of compression behavior of 3D printed lattice structures, Addit Manuf 54 (2022). https://doi.org/10.1016/j.addma.2022.102774.